

Spin-orbit interactions in black-hole binaries

M. Campanelli, C. O. Lousto, and Y. Zlochower

*Department of Physics and Astronomy, and Center for Gravitational Wave Astronomy,
The University of Texas at Brownsville, Brownsville, Texas 78520*

(Dated: December 2, 2024)

We perform numerical simulations of black-hole binaries to study the exchange of spin and orbital angular momentum during the last, highly nonlinear, stages of the coalescence process. To calculate the transfer of angular momentum from orbital to spin, we start with two quasi-circular configurations, one with initially non-spinning black holes, the other with corotating black holes. In both cases the binaries complete almost two orbits before merging. We find that, during these last orbits, the specific spin (a/m) of each horizon increases by only 0.012 for the initially non-spinning configuration, and by only 0.006 for the initially corotating configuration. By contrast, the corotation value for the specific spin should increase from 0.1 at the initial proper separation of $10M$ to 0.33 when the proper separation is $5M$. Thus the spin-orbit coupling is far too weak to tidally lock the binary to a corotating state during the late-inspiral phase. We also study the converse transfer from spin into orbital motion. In this case, we start the simulations with parallel, highly-spinning non-boosted black holes. As the collision proceeds, the system acquires a non-head-on orbital motion, due to spin-orbit coupling, that leads to the radiation of angular momentum. We are able to accurately measure the energy and angular momentum losses and model their dependence on the initial spins.

PACS numbers: 04.25.Dm, 04.25.Nx, 04.30.Db, 04.70.Bw

I. INTRODUCTION

With the advent of new methods to evolve black-hole binaries for several orbits [1, 2, 3, 4, 5, 6, 7] we can now pose questions of physical interest about the details of their interactions and the generation of gravitational radiation, and find answers that allow us to better understand the astrophysical properties of black-hole binaries.

The coalescence of unequal-mass black-hole binaries with randomly oriented individual spins is expected to be one of the strongest astrophysical sources of gravitational radiation. The first numerical simulations of non-spinning unequal-mass black-hole binaries, along with the calculation of the merger kicks, were reported in Refs. [8, 9, 10].

In a preceding paper [11] we performed the first fully-nonlinear simulations of highly spinning black-hole binaries and showed that the spin-orbit coupling leads to significant changes in the orbital dynamics, as well as gravitation radiation emitted, in the final stages of a black-hole binary. In this paper we study in more detail the mechanisms that transfer orbital angular momentum to spin and *vice versa*.

It is of astrophysical interest to know if tidal effects could lock the spin of black-hole binaries to a corotating state, i.e. a state where the spins of the individual horizons are aligned with orbital angular momentum, and the spin magnitudes are such that the horizon frequency Ω_H (Ω_H is the angular speed of locally-non-rotating observers as they pass through the horizon, as seen by stationary observers at infinity) is nearly equal to the orbital frequency Ω_O . For a Kerr hole with mass m and specific

spin a/m the horizon frequency takes the value

$$\Omega_H = \frac{1}{2m} \left(\frac{a/m}{1 + \sqrt{1 - (a/m)^2}} \right). \quad (1)$$

See Ref. [12] for a first post-Newtonian (1PN) correction to the corotation condition $\Omega_O = \Omega_H$. Note that in this paper we consider both the spin (or more accurately, the spin angular momentum) S of a black hole, which has units of M^2 , and the specific-spin a/m (m is the horizon mass), which is dimensionless. The two are related by $S = am$. We will also make use of the following relationships between the spin, specific spin, horizon frequency, and irreducible mass (m_{IR}):

$$S = \frac{4m_{\text{IR}}^3 \Omega_H}{\sqrt{1 - 4(m_{\text{IR}} \Omega_H)^2}}, \quad (2)$$

$$a/m = 4m_{\text{IR}} \Omega_H \sqrt{1 - 4(m_{\text{IR}} \Omega_H)^2}, \quad (3)$$

where $16\pi m_{\text{IR}}^2$ is the horizon surface area.

There are two competing scales in this problem: one is the time for tidal effects to act to spin up (or down) the black holes to the orbital frequency and the other is the rate of change of the orbital frequency due to gravitational radiation.

In the early stages of the orbital motion of black-hole binaries, tidal effects are small and can be described by Newtonian theory; these effects decay strongly with the binary separation r (as μ/r^3 , with μ the reduced mass of the system). Tidal effects will be stronger as the holes get closer, but this will also increase the orbital frequency (roughly like $\Omega_O \sim \sqrt{\mu/r^3}$). In order to be correctly quantified, these effects need to be evaluated dynamically with a fully non-linear numerical simulation of the

final orbital stage of black-hole binaries. Despite this, several computations of quasi-circular sequences of initial data for black-hole binaries have assumed corotating spins from larger separations down to the estimated location of the innermost stable circular orbit (ISCO) [12, 13, 14]. Corotation has a notable effect on the location of the ISCO in all these calculations; fortunately, recent numerical evolutions of equal-mass black-hole binaries [4, 5, 6] do not find any particular physical effect associated with the location of the ISCO.

Bildsten and Cutler [15] (see also [16]) studied neutron star (NS) and black hole (BH) systems. They conclude that, for the NS-NS binary the viscosity is too low to tidally synchronize the stars as they inspiral, and that there is simply not enough time during the gravitational radiation driven inspiral of NS-BH binaries to tidally lock the spin of the neutron star to the orbital period. Additionally, when the NS-BH binaries are close enough for the tidal effects to be strong, the neutron stars are disrupted in a few orbits. Since these arguments do not strictly apply to black-hole binaries, it is interesting to explore these tidal interactions dynamically with fully non-linear numerical techniques. This spin-up of NS-NS binaries has also been analyzed in Ref. [17].

We will study in Sec. III the tidal spin-up of two equal-mass, initially non-spinning, black holes starting from a quasi-circular orbit (as determined by 3PN trajectories) with nearly two orbits left before merger, as well as a similar configuration with initially corotating black holes. These equal-mass configurations involving the very last stages of the inspiral should nearly maximize the tidal effects.

While the transfer of orbital angular momentum to the spin of the members of a binary system is of astrophysical relevance, we can also study the conversion of spin into orbital angular momentum and verify the importance of its dynamical effects. To this end, we evolve binaries consisting of non-boosted, equal-mass black holes, with the black holes aligned along the y -axis and the individual spins aligned along the $+z$ -axis, and measure the radiated energy and angular momentum. This simple set-up clearly displays the transfer of spin to orbital motion. For non-spinning holes this set-up produces purely head-on collisions, leading to the radiation of energy but *not* angular momentum. For spinning holes, the spin-orbit coupling causes the holes to acquire non-head-on orbital motion, leading to the radiation of angular momentum. Thus, an accurate measure of the angular momentum radiated would allow us to estimate the correct magnitude of this effect.

The leading post-Newtonian spin-orbit and spin-spin corrections to the acceleration of two equal-mass black holes (each of mass m), with spins \vec{S}_1 and \vec{S}_2 perpendicular to the motion, in a nearly head-on collision are:

$$\vec{a}_{SO} = -\frac{18}{r^3}(\vec{v}_r \times (\vec{S}_1 + \vec{S}_2)), \quad (4)$$

$$\vec{a}_{SS} = -\frac{6}{mr^4}(\vec{S}_1 \cdot \vec{S}_2)\hat{r}, \quad (5)$$

where \vec{r} is the binary separation, \vec{v}_r is the relative velocity, and SO and SS denote spin-orbit and spin-spin coupling terms respectively. While the spin-spin acceleration adds an attractive term along the radial direction (for parallel spins; repulsive for anti-parallel), the spin-orbit acceleration is perpendicular to both the mostly-radial (along \hat{r}) head-on velocity and the spin, and hence leads to a non-vanishing orbital component of the binary motion.

In Sec. IV we will study this nonlinear coupling using fully non-linear numerical evolutions and show that our method is able to extract meaningful results for this numerically demanding relatively small effect.

II. TECHNIQUES

We use the Brandt-Brügmann puncture approach [18] along with the TwoPUNCTURES [19] and BAM_ELLIPTIC [20] thorns to compute initial data. In this approach the 3-metric on the initial slice has the form $\gamma_{ab} = (\psi_{BL} + u)^4\delta_{ab}$, where ψ_{BL} is the Brill-Lindquist conformal factor, δ_{ab} is the Euclidean metric, and u is (at least) C^2 on the punctures. The Brill-Lindquist conformal factor is given by $\psi_{BL} = 1 + \sum_{i=1}^n m_i/(2r_i)$, where n is the total number of ‘punctures’, m_i is the mass parameter of puncture i (m_i is *not* the horizon mass associated with puncture i), and r_i is the coordinate distance to puncture i . In all cases below, we evolve data containing only two punctures with equal puncture mass parameters, and we denote this puncture mass parameter by m_p . We evolve these black-hole-binary data sets using the LAZEv [21] implementation of the moving puncture approach [2, 3]. In our version of the moving puncture approach [2] we replace the BSSN [22, 23, 24] conformal exponent ϕ , which has logarithmic singularities at the punctures, with the initially C^4 field $\chi = \exp(-4\phi)$. This new variable, along with the other BSSN variables, will remain finite provided that one uses a suitable choice for the gauge. An alternative approach uses standard finite differencing of ϕ [3]. Note that both approaches have been used successfully by several other groups [9, 25, 26].

We obtain accurate, convergent waveforms and horizon parameters by evolving this system in conjunction with a modified 1+log lapse, a modified Gamma-driver shift condition [2, 27], and an initial lapse $\alpha \sim \psi_{BL}^{-4}$. The lapse and shift are evolved with $(\partial_t - \beta^i \partial_i)\alpha = -2\alpha K$, $\partial_t \beta^a = B^a$, and $\partial_t B^a = 3/4\partial_t \tilde{\Gamma}^a - \eta B^a$. These gauge conditions require careful treatment of χ near the puncture in order for the system to remain stable [2, 4]. In Ref. [28] it was shown that this choice of gauge leads to a strongly hyperbolic evolution system provided that the shift does not become too large. For our version of the moving puncture approach, we find that the product $\alpha \tilde{A}^{ij} \partial_j \phi$ initially has to be C^4 on the puncture. In the spinning case, \tilde{A}^{ij} is $O(r^3)$ on the puncture, thus requiring that $\alpha \propto r^3$ to maintain differentiability. We therefore choose

an initial lapse $\alpha(t=0) = 2/(1+\psi_{BL}^4)$ which is $O(r^4)$ and C^4 on the puncture and reproduces the isotropic Schwarzschild lapse at large distances from the horizons. The initial values of β^i and B^i are set to zero.

Hannam et. al. [26] examine the smoothness of the evolved fields at late times at the puncture. They find that, in the case of Schwarzschild, χ transitions from an initially C^4 field to a C^2 field at late times. Although we require that the fields are initially C^4 , this late-time drop in smoothness does not appear to leak out of the horizon (which is consistent with the analysis in [26]).

We use a ‘multiple transition’ fisheye transformation [4] to push the boundaries to $100M$, while maintaining a resolution of up to $M/40$ in the central region, for the head-on runs; for orbital runs we push the boundaries to $215M$, with a central resolution of up to $M/31.5$.

We use a locally modified version of the AHFINDERDIRECT thorn [29] to find the individual apparent horizon, and we measure the angular momentum of the horizons using our implementation of the isolated horizon algorithm detailed in [30]. (The isolated horizon formalism used here is extended to the dynamical case in [31].) In the isolated horizon approach, the horizon spin is given by

$$S = \frac{1}{8\pi} \oint_{AH} (\varphi^a R^b K_{ab}) d^2V. \quad (6)$$

where φ^a is an approximate Killing vector on the horizon, K_{ab} is the extrinsic curvature, d^2V is the natural area element intrinsic to the horizon, and R^a is the outward pointing unit vector normal to the horizon on the 3D slice. (See appendix A for a comparison of the isolated horizon technique for finding the horizon spin to the more common horizon circumference technique.) We confirm that our version of the algorithm produces the correct spin for various coordinate distortions of Kerr, as well as for Bowen-York binary initial data (both with and without linear momentum).

We measure the proper distance between the horizons by shooting geodesics from the origin to a horizon, and then finding the geodesic with the minimum proper distance as described in Refs. [32, 33] (the proper distance between the two holes is then double this distance). This technique will work in cases where there is (at least) Pi -symmetry on the equatorial plane and reflection symmetry across the plane.

III. TIDAL SPIN-UP OF BLACK-HOLE BINARIES

The spin of the individual horizons in a black-hole binary will become tidally locked to the orbital frequency if the non-linear spin-orbit coupling is sufficiently strong that the timescale for tidally induced spin-up (or down) is smaller than the timescale for change in the orbital period. In order to obtain an accurate measure of the strength of this coupling we examine the cases of initially

TABLE I: Initial data for quasi-circular, equal-mass black-hole binaries. The binaries have an ADM mass of $(1.0000 \pm 0.0005)M$, with orbital frequency $M\Omega$ fixed to 0.500, total angular momentum (orbital + spin) given by $(0, 0, J)$, and proper horizon separation l . The punctures are located at $(0, \pm Y, 0)$, with mass parameter m_p , momentum $(\mp P, 0, 0)$, spin angular momentum $(0, 0, S)$, and specific spin a/m (m is the horizon mass).

Name	S/M^2	Y/M	P/M	J/M^2	a/m	m_p/M	l/M
S0	0.000	3.280	0.1336	0.876	0.0000	0.4848	10.01
SC	0.025757	3.2534	0.1330	0.917	0.1001	0.4831	9.93

non-spinning and initially corotating close binaries, denoted by S0 and SC respectively, where the binary separation is small enough that the spin-orbit coupling is large, but large enough that the binaries complete at least ~ 1.75 orbits before merging. The initial data parameters for these configuration are provided in Table I and have been obtained by finding quasi-circular orbits with the 3PN equations of motion. We originally studied the S0 non-spinning configuration in Ref. [11]. While in [11] we were interested in the spin of the remnant horizon and plunge times as a function of the initial spin of the individual horizons, here we are interested only in the pre-merger spin-up of the individual horizons. It is then crucial to have an appropriate measure of the individual spin of the holes. We employ the isolated horizon spin algorithm detailed in [30] (see Eq. (6)). Strictly speaking, isolated horizon techniques are only valid for non-interacting horizons. However, they do provide an excellent approximation to the horizon spin even in the case of relatively close binaries. We confirmed that our implementation gives accurate evaluations of the horizon spins for closely separated Bowen-York binary data. For this test we constructed a sequence of initial data using the TWOPOUNCTURES thorn [19] with fixed orbital angular momentum $L = 0.876M^2$ (the value for the S0 case above) and ADM mass of $(1.0000 \pm 0.0005)M$. We set the spin of the individual holes (aligned along the $+z$ -axis) to $S = 0M^2$, $S = 0.001M^2$, and $S = 0.0001M^2$, and measured the spins of the horizons with our implementation of the isolated horizon algorithm. The results of these calculations are summarized in Table II. From the table we see that spins as low as $10^{-4}M^2$ can be measured with an accuracy of better than 20% even when the holes are separated by a proper distance of $l \sim 3M$, and can be measured with an accuracy of 1% or better when the holes are separated by $l \geq 4.6M$. Interestingly, accurate measurement of this spin can be obtain even with coordinate separations as small as $0.5M$.

We evolved the S0 and SC configurations with 3 different resolutions, $h = M/22.5$, $h = M/27$, and $h = M/31.5$, where h is the central grid-spacing, and calculated the horizon spins after every $1M$ of evolution. The results of measuring the spin of the individual holes during the orbital motion until the formation of a common

TABLE II: The isolated horizon spin of a sequence of Bowen-York data with given spins and ADM mass (1.0000 ± 0.0005) M . Here $(\pm x, 0, 0)$ are the coordinate locations of the punctures, S is the measured spin (the Bowen-York spin parameter is given in parentheses), and l is the proper distance between horizons. In all cases the linear momentum is given by $\vec{P} = (0, \pm 0.8764M^2/(2x), 0)$ (to reproduce the S0 orbital angular momentum), and the spins are aligned with the z -axis.

x/M	$S/M^2(10^{-3})$	$S/M^2(10^{-4})$	$S/M^2(0)$	l/M
3.280	1.000×10^{-3}	1.003×10^{-4}	3.0×10^{-7}	10.0
3.0	1.011×10^{-3}	1.011×10^{-4}	1.1×10^{-6}	9.4
2.0	9.998×10^{-4}	9.97×10^{-5}	3.4×10^{-7}	7.0
1.0	1.001×10^{-3}	1.011×10^{-4}	1.13×10^{-6}	4.6
0.5	1.01×10^{-3}	1.11×10^{-4}	1.08×10^{-5}	3.4
0.25	1.02×10^{-3}	1.17×10^{-4}	1.7×10^{-5}	3.0

TABLE III: Merger time, T_{CAH}/M , for the S0 and SC configurations versus resolution. Horizon searches were performed every $0.3M$ and $0.2M$ for the S0 and SC configuration respectively.

resolution	S0	SC
$M/22.5$	160.7 ± 0.3	168.6 ± 0.2
$M/27$	166.0 ± 0.3	174.2 ± 0.2
$M/31.5$	168.3 ± 0.3	176.6 ± 0.2
extrapolation	172 ± 2	179 ± 2

apparent horizon (CAH) (See Table III) for the S0 configuration are displayed in Fig. 1, while the results for the SC configuration are displayed in Fig. 2. The upper panel in both figures shows the specific spin of the individual holes for the three resolutions. We observe that in both cases the specific-spin increase during the evolution is small (0.012 for S0 and 0.006 for SC). The lower panels show essentially third-order convergence as expected from our use of third-order-accurate interpolators with AHFINDERDIRECT. The late-time error in the S0 specific spin for the lowest resolution run appears to show a very large error compared to the actual value of the specific spin. This ‘error’ is actually a phase error resulting from the lower resolution runs merging sooner. However, in a specific spin versus proper separation plot, the curves from all three resolutions lie on top of each other (see Fig. 3) at late-times (i.e. at small proper distance). This dichotomy, between the late-time convergence break-down of a/m versus t and the excellent late-time agreement between resolutions in a/m versus l , is similar to the results previously seen in the waveforms of inspiraling binaries [5, 11, 34]. In that case it was observed that $\psi_4(t)$ lost convergence due to large phase errors induced by the lower resolution runs merging sooner, while the phase-corrected ψ_4 showed excellent agreement between resolutions. In this case the ‘phase error’ is in $l(t)$, and by plotting a/m versus l we effectively removed the phase error.

The values that we obtained for the spin-up of the

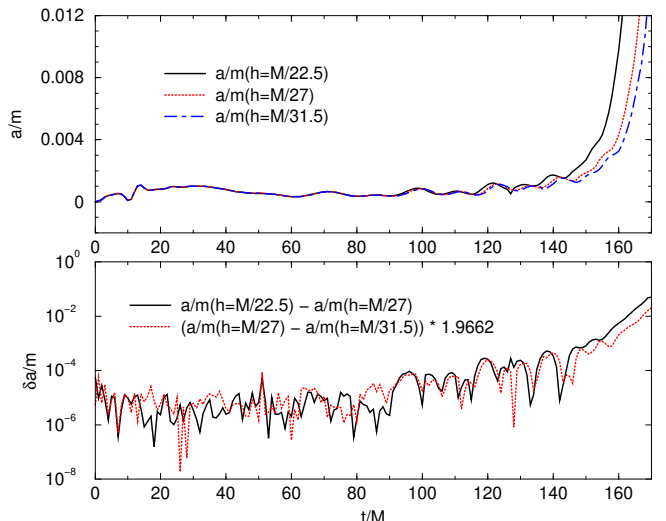


FIG. 1: The measured instantaneous specific spin of the individual horizons, for the S0 configuration, starting from vanishing spin at $t = 0$ and up to the merger time. The top panel shows a/m versus time for three resolutions with grid-spacings $h = M/22.5$, $h = M/27$, and $h = M/31.5$, while the lower panel shows the differences in a/m between the low and medium resolutions and the medium and high resolutions (the latter rescaled by 1.9662 to demonstrate third-order convergence). The differences between the low and medium resolutions and medium and high resolutions become large at late times due to the lower resolution runs merging sooner. The curves in the top panel have been cut off at the approximate merger value of a/m (which is independent of resolution).

binary holes are much smaller than those expected for a corotation state [43]. In order to visualize this we have displayed in Fig. 4 the measured spin during the orbital motion, this time against the proper separation of the apparent horizons. The S0 configuration forms a common apparent horizon (CAH) at a proper separation of $l_{CAH} = 1.75M$, while the SC configuration forms a common apparent horizon at a proper separation of $l_{CAH} = 1.69M$. In order to have a measure of what the corresponding corotation spin is, we considered the family of corotating binaries in quasi-equilibrium of Ref. [14] (we have used Eq. (3) to convert the Ω_H and m_i provided in [14] into a/m). From the plot we see that the SC is initially corotating, but the specific spin remains flat for most of the run. Thus the spin-orbit coupling is far too small to keep this system tidally locked. It is interesting to note that the spin-up for the S0 configuration is slightly larger than the spin-up for the SC configuration. Both configuration show essentially no spin-up above proper separations of $\sim 4M$.

The relatively low ‘spin up’ that we measure during the last couple of orbits prior to the merger indicates that the time-scale for tidal locking is much larger than the time-scale of orbital decay due to gravitational radiation emission. We also note that in the leading relevant post-

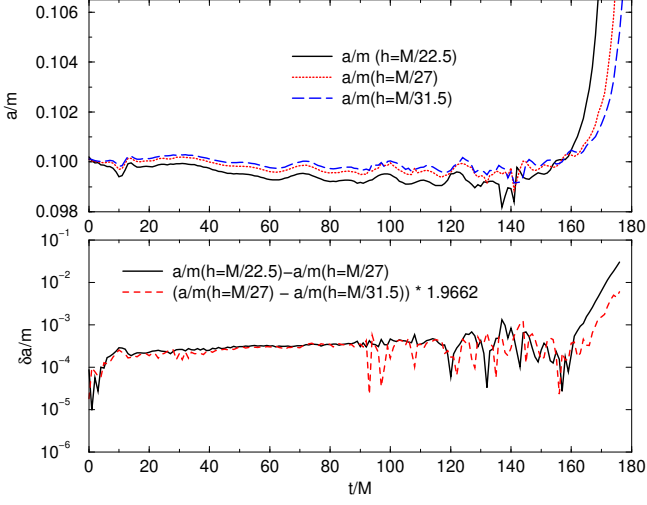


FIG. 2: The measured instantaneous specific spin of the individual horizons, for the SC configuration, starting from $a/m = 0.1$ at $t = 0$ and up to the merger time. The top panel shows a/m versus time for three resolutions with grid-spacings $h = M/22.5$, $h = M/27$, and $h = M/31.5$, while the lower panel shows the differences in a/m between the low and medium resolutions and the medium and high resolutions (the latter rescaled by 1.9662 to demonstrate third-order convergence). The differences between the low and medium resolutions and the medium and high resolutions become large at late times due to the lower resolution runs merging sooner. The curves in the top panel have been cut off at the approximate merger value of a/m (which is independent of resolution).

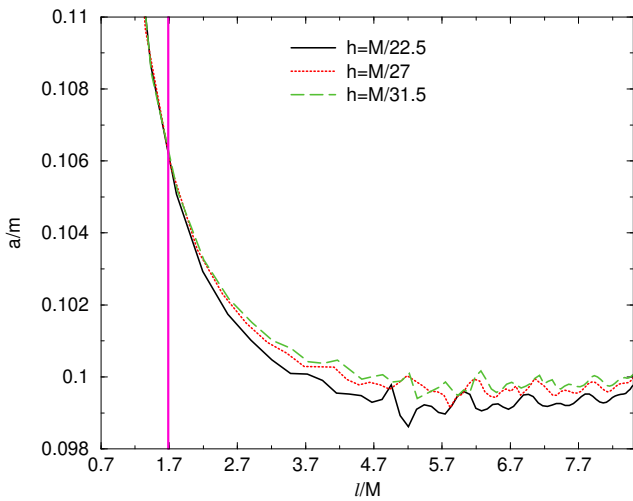


FIG. 3: The specific spin a/m for the SC configuration versus proper binary separation l for three resolutions with grid-spacings $h = M/22.5$, $h = M/27$, and $h = M/31.5$. Note that the large late-time phase errors seen in a/m versus time are not present in this plot. The vertical line shows the proper distance at merger.

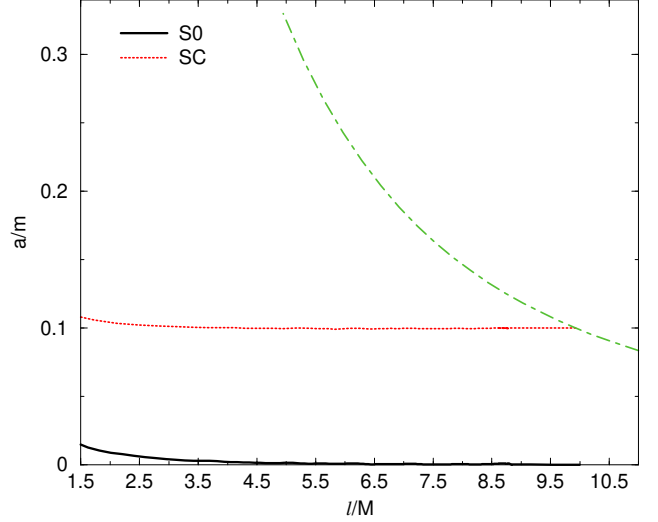


FIG. 4: The spin-up of the horizons versus proper binary separation. The continuous line shows a/m for the S0 configuration, the dotted line shows a/m for the SC configuration (initially corotating), and the dot-dash line shows the corotation value for the spin. Note that the S0 configuration shows a slightly larger spin-up and that both spin-ups are much smaller than what is required to tidally lock the binary.

Newtonian order, the change of the spin, averaged over a circular orbit, which is given by [35]

$$\dot{\vec{S}}_i = \frac{1}{2r^3} \left\{ (\vec{L}_N \times \vec{S}_i)(4 + 3\frac{m_j}{m_i}) + \vec{S}_j \times \vec{S}_i - 3(\hat{L}_N \cdot \vec{S}_j)\hat{L}_N \times \vec{S}_i \right\} \quad (j \neq i), \quad (7)$$

vanishes for all configurations with the spins aligned with the orbital angular momentum. In Eq. (7) \vec{L}_N is the (Newtonian) orbital angular momentum, \vec{S}_i is the spin of black hole i , m_i is its mass, and j denotes the other black hole. Will [36] also points out that the radiation reaction interaction does not modify the spin up to 3.5PN order. First effects of the flattening of the bodies should actually be seen at 4.5PN order.

IV. SPIN-ORBIT COUPLINGS IN BLACK-HOLE BINARIES

We continue our study of the relevance of spin-orbit coupling to the orbital dynamics of black-hole binaries by choosing initially head-on (vanishing transverse linear momentum) configurations that single out the converse transfer of spin into orbital angular momentum. Purely head-on collisions do not radiate angular momentum to infinity. Thus, in these configurations, the radiated angular momentum is an indicator of the extent to which these systems deviate from head-on motion (i.e. the extent to which they acquire transverse motion). The energy and

TABLE IV: Initial data for non-boosted black-hole binaries. The binaries have an ADM mass of $(1.0000 \pm 0.00005)M$, with total angular momentum $(0, 0, J)$, and proper horizon separation l . The punctures are located at $(0, \pm Y, 0)$, with mass parameter m_p , spins angular momentum $(0, 0, S)$, and specific spin a/m (here m is the horizon mass).

Name	S/M^2	Y/M	P/M	J/M^2	a/m	m_p/M	l/M
HS++	0.200	4.000	0.000	0.4	0.7581	0.3444	12.24
MS++	0.100	4.2422	0.000	0.2	0.3775	0.469755	12.24
0S++	0.000	4.2924	0.000	0.0	0.0000	0.5000	12.24

angular momentum radiated are functions of the spins of the two horizons, the initial inward momentum of each hole, and the proper separation. To simplify the analysis, we choose head-on binaries with zero initial linear momentum and with a fixed initial proper separation of $12.24M$. All spins are aligned along the z -axis, with the binaries initially separated along the y -axis. We report the initial data parameters in Table IV.

We measure the radiated energy and angular momentum by solving for the final hole remnant horizon mass and spin, and then subtracting these quantities from the ADM mass and angular momentum (as determined from the initial data). To avoid confusion with the initial black-hole mass and spins, we denote the mass and spin of the final remnant horizon with M_H and J_H respectively. The radiated mass and angular momentum then are:

$$E_{rad} = M_{ADM} - M_H, \quad (8)$$

$$J_{rad} = J_{ADM} - J_H, \quad (9)$$

where in these head-on cases J_{ADM} is the sum of the spins of the two initial black holes. For notational convenience we introduce the symbol j_0 defined by

$$j_0 = \frac{J_{ADM}}{M_{ADM}^2}. \quad (10)$$

In previous papers [4, 11] we found that the horizon provided a very accurate measurement of these quantities. Additionally, when using isolated horizon techniques, we can obtain the horizon parameters accurately within $30M$ after the merger. In all cases the radiated energy and angular momentum are very small. In order to accurately obtain these numbers we need to evolve all configurations at three different resolutions (see Table V for the grid-spacings) and then use a Richardson extrapolation of the radiated energy and angular momentum. The measured convergence rates for the radiated angular momentum are 3.9 and 3.7 for the HS++ and

MS++ configurations respectively, while the measured convergence rates for the radiated energy are 4.0, 3.7, and 3.9 for the HS++, MS++, and 0S++ configurations respectively. The lower convergence rates for the MS++ configuration may simply indicate only that higher resolution is needed. Alternatively it is possible that small third-order errors (possibly from the interpolators) are present in all configurations, but are only observed in the MS++ configuration due to its finer effective resolution. (The effective grid-spacing is $h_{eff} = h/m_p$, where h is the actual grid-spacing and m_p is the puncture mass parameter (see [11] for details)). For the Richardson extrapolation we use both the forms $f(h) = f_\infty + e h^4 + g h^5$ and $f(h) = f_\infty + d h^3 + e h^4$, and, using results from the three resolutions, solve for f_∞ . We take the difference between these two extrapolation to be indicative of the error in our extrapolated numbers. In Figures 5 and 6 we show the HS++ final remnant black-hole horizon mass and spin versus time for three resolutions, as well as the two extrapolations of these quantities and convergence plots. It is evident from the very close agreement between the two extrapolations that we obtain highly accurate measurements of both the horizon mass and spin, and consequently, the radiated mass and angular momentum.

In Table V we summarize the results for these configurations. Note that the errors reported in the table for a given resolution are of the uncertainty in measurement of J_H and M_H at that resolution (i.e. a measure of the flatness of the late-time plateaus of J_H and M_H). Thus the error interval reported for e.g. J radiated at a resolution of $M/25$ will not necessarily contain the final extrapolated value. On the other hand, the error intervals for the extrapolated values are our best estimate for the true value of each quantity. A fit of the Richardson-extrapolated values of the radiated angular momentum to the initial spins of the individual black holes has the form:

$$\frac{J_{rad}}{M^2} = (4.8 \pm 0.1) \times 10^{-3} j_0 + (4.0 \pm 0.9) \times 10^{-3} j_0^3 + O(j_0^5), \quad (11)$$

where $j_0 = 2S/M_{ADM}^2$ (see Table IV). The linear term is the dominant one for these configurations (the HS++ configuration radiates $\sim 20\%$ more momentum than expected from the linear behavior alone). Equation (11) contains only odd powers of j_0 since the magnitude of J_{rad} must be independent of j_0 (i.e. the physics would not change if the two spins were aligned along the $-z$ -axis), and the sign of J_{rad} must match the sign of j_0 .

An analysis of the radiated energy versus spin is com-

plicated by the fact that the binary radiates energy in

TABLE V: The radiated mass and angular momentum as well as the merger time (T_{CAH}) and final specific spin for the head-on configurations. The reported error intervals in T_{CAH} are a function of how often a horizon search was performed. In all cases T_{CAH} does not appear to vary with resolution.

Case	resolution	E_{rad}/M_{ADM}	J_{rad}/J_{ADM}	T_{CAH}/M	a/M_H
HS++	M/25	$(0.16 \pm 0.02)\%$	$(2.37 \pm 0.02)\%$	36.7 ± 0.2	0.3918 ± 0.002
	M/30	$(0.136 \pm 0.009)\%$	$(1.44 \pm 0.01)\%$	36.6 ± 0.2	0.39532 ± 0.00008
	M/40	$(0.123 \pm 0.004)\%$	$(0.832 \pm 0.003)\%$	36.7 ± 0.2	0.39765 ± 0.00003
	extrapolation	$(0.118 \pm 0.002)\%$	$(0.546 \pm 0.002)\%$	36.7 ± 0.2	0.39876 ± 0.00002
MS++	M/25	$(0.065 \pm 0.004)\%$	$(1.038 \pm 0.008)\%$	39.5 ± 0.2	0.19817 ± 0.00003
	M/30	$(0.063 \pm 0.003)\%$	$(0.7698 \pm 0.0040)\%$	39.6 ± 0.2	0.19868 ± 0.00003
	M/35	$(0.062 \pm 0.002)\%$	$(0.6567 \pm 0.0069)\%$	39.5 ± 0.2	0.19891 ± 0.00003
	extrapolation	$(0.060 \pm 0.002)\%$	$(0.4986 \pm 0.0086)\%$	39.5 ± 0.2	0.19920 ± 0.00007
0S++	M/22.5	0.0616 ± 0.0032	0	40.4 ± 0.2	0
	M/25	$(0.0595 \pm 0.0025)\%$	0	40.4 ± 0.2	0
	M/30	$(0.057 \pm 0.002)\%$	0	40.4 ± 0.2	0
	extrapolation	$(0.054 \pm 0.002)\%$	0	40.4 ± 0.2	0

the zero-spin configuration as well. After subtracting the zero-spin radiated energy we find that the HS++ configuration radiates $0.064 \pm 0.003M$ more energy than the zero-spin configuration, while the MS++ configuration only radiates $0.006 \pm 0.002M$ more. Thus the HS++ configuration radiates 12.2 ± 4.6 times as much as the MS++ configuration (after subtracting off the zero-spin radiated energy). From these results it appears that the radiated energy scales with j_0^3 or j_0^4 . A close-limit analysis (See Eq. (19)) also indicates that there is a small j_0^2 contribution as well. Although not obvious in the total radiated energy, this quadratic dependence on J can be seen in the imaginary part of the ($\ell = 2, m = \pm 2$) components of the radiated energy $E(t)$ (i.e. the amount of radiation emitted up to time t), where $E(t) = \sum_{\ell,m} (R_{\ell m}(t) + I_{\ell m}(t))$,

$$R_{\ell m}(t) = \frac{1}{4\pi} \int_0^t Re[N_{\ell m}(\tau)]^2 d\tau, \quad (12)$$

$$I_{\ell m}(t) = \frac{1}{4\pi} \int_0^t Im[N_{\ell m}(\tau)]^2 d\tau, \quad (13)$$

$N_{\ell m}(t) = (r - 2M)/2 \int_0^t \bar{\psi}_{4,\ell m}(\tau) d\tau$, and ψ_4 is calculated using the quasi-Kinnersley tetrad method [37]. Figure 7 shows $R_{\ell m}(t)$ and $I_{\ell m}(t)$ for the $\ell = 2$ components of the waveform for the HS++ and MS++ configurations. Note that $I_{2\pm 2}$ (which vanishes in the zero-spin case) is 4.3 times larger in the HS++ configuration than in the MS++ configuration. This is consistent with a quadratic dependence on the spin plus smaller higher-order dependencies.

Finally, if we fit the radiated energy to the polynomial dependence $E_0 + E_2 j_0^2 + E_4 j_0^4$ we obtain

$$\begin{aligned} \frac{E_{rad}}{M} = & (0.052 \pm 0.02) + (0.065 \pm 0.033)j_0^2 \\ & + (2.08 \pm 0.21)j_0^4 + O(j_0^6). \end{aligned} \quad (14)$$

Note that the coefficient of the quadratic term is two orders of magnitude smaller than the coefficient of the quartic term (and thus was not apparent in our initial

analysis above). There are only even terms in Eq. (14) because the E_{rad} cannot depend on the sign of j_0 (i.e. E_{rad} must be the same for configurations with the spins aligned on the $+z$ -axis and with the spins aligned on the $-z$ -axis).

The Bowen-York initial data family contains ‘spurious’ radiation that does not represent any physical history of the binary. In addition, the spinning case does not have the Kerr limit when the two black holes are far apart. (For a data set with the right Kerr limit see [38, 39].) While this extra radiation is of relatively small magnitude in orbiting black-hole binaries (See [11]), it is relevant in the highly spinning head-on collisions considered here. This can be observed in Fig. 7. The first plateau in the radiated energy ($t = 40M - 70M$) for the observer location at $r = 35M$ is due to the radiated ‘spurious’ energy. This ‘spurious’ energy contributes up to 25% of the total energy radiated of the HS++ configuration, but strongly decreases for the MS++ and 0S++ configurations.

One can use the lowest relevant post-Newtonian expansion to support (qualitatively) our results. A look at the Post-Newtonian equations of motion [35] shows that the leading spin-orbit interaction is of 1.5PN order, while the leading spin-spin interaction is of 2PN order. Kidder [35] gives the radiated energy and momenta of the point-particle spin-orbit and spin-spin couplings up to 2PN order. The relevant equations for our nearly head-on collisions are:

$$\dot{E}_N = -\frac{8\bar{m}^4}{15r^4} v_r^2, \quad (15a)$$

$$\dot{E}_{PN} = -\frac{2\bar{m}^4}{105r^4} \left\{ -110v_r^4 + 452\frac{\bar{m}}{r}v_r^2 \right\}, \quad (15b)$$

$$\dot{E}_{SO} = 0, \quad (\vec{L}_N = 0), \quad (15c)$$

$$\dot{E}_{SS} = \frac{32\bar{m}^2}{5r^6} (\vec{S}_1 \cdot \vec{S}_2) v_r^2, \quad (15d)$$

where r is the binary separation, $2\bar{m} = m_1 + m_2$, \vec{v}_r is the relative velocity, N denotes Newtonian terms, PN denotes (non-spin-orbit and non-spin-spin) post-Newtonian

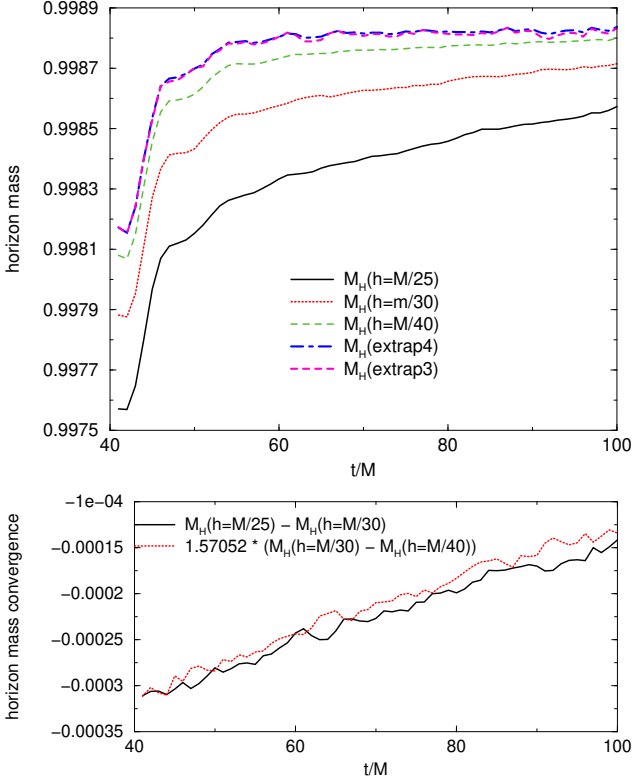


FIG. 5: The final remnant horizon mass versus time for the HS++ configuration. The top panel shows the horizon mass for the three resolutions with grid-spacings $h = M/25$, $h = M/30$, and $h = M/40$, and the two Richardson extrapolations based on leading third-order and leading fourth-order errors. The bottom panel shows the differences in the horizon mass for the $h = M/25$ and $h = M/30$ runs as well as the differences in the mass for the $h = M/30$ and $h = M/40$ runs. This latter difference is rescaled by 1.57052 to demonstrate 3.7-order convergence. The accurate extrapolations (as evident by the agreement of the two extrapolations) to infinite resolution allows for a sufficiently precise determination of the radiated energy to model its dependence on the initial spins.

terms, SO denotes spin-orbit coupling terms, and SS denotes spin-spin coupling terms. Note that the lowest-order spin-correction to the radiated energy is quadratic in S . Likewise we can obtain the radiated angular momentum

$$\vec{J}_N = 0, \quad (\vec{L}_N = 0), \quad (16a)$$

$$\vec{J}_{PN} = 0, \quad (\vec{L}_N = 0), \quad (16b)$$

$$\vec{J}_{SS} = 0 \quad (\vec{a}_N \sim \vec{a}_{SS} \sim \hat{r}), \quad (16c)$$

$$\begin{aligned} \vec{J}_{SO}^{++} &= -\frac{4\bar{m}^2}{15r^3} \vec{v}_r \times (\vec{v}_r \times (\vec{S}_1 + \vec{S}_2)) \\ &\quad \left\{ v_r^2 + \frac{2\bar{m}}{r} + \frac{1}{v_r^2} \frac{4\bar{m}^2}{r^2} \right\}, \end{aligned} \quad (16d)$$

which displays the leading linear dependence on the spin,

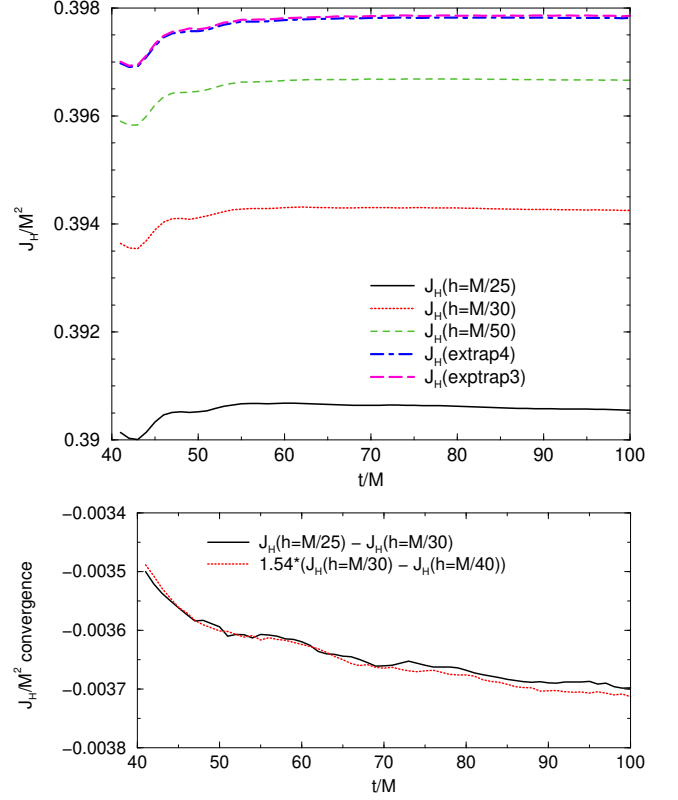


FIG. 6: The angular momentum of the final remnant black hole for the HS++ configuration measured by the isolated horizon method. The top panel shows the horizon spin for the three resolutions with grid-spacing $h = M/25$, $h = M/30$, and $h = M/40$, as well as the two Richardson extrapolations based on leading third-order and leading fourth-order errors. The bottom panel shows the differences in the horizon spin for the $h = M/25$ and $h = M/30$ runs as well as the differences in the spin for the $h = M/30$ and $h = M/40$ runs. This latter difference is rescaled by 1.54 to demonstrate 4th-order convergence. The accurate extrapolations (as evident by the agreement of the two extrapolations) to infinite resolution allows for a sufficiently precise determination of the radiated angular momentum to model its dependence on the initial spins.

and the radiated linear momentum

$$\vec{P}_N = 0, \quad (\delta m = m_1 - m_2 = 0) \quad (17a)$$

$$\vec{P}_{PN} = 0, \quad (\delta m = m_1 - m_2 = 0) \quad (17b)$$

$$\vec{P}_{SS} = 0 \quad (\text{at this order}) \quad (17c)$$

$$\begin{aligned} \vec{P}_{SO}^{++} &= -\frac{8\bar{m}^3}{15r^5} v_r (\vec{v}_r \times \vec{\Delta}) = 0, \\ &\quad (\vec{\Delta} = 2(\vec{S}_1 - \vec{S}_2) = 0). \end{aligned} \quad (17d)$$

Note that equation (17d) gives a non-vanishing linear momentum radiated for anti-parallel spins. The spin-orbit interaction is the only one that reverses signs when spins change signs. This explains the different stability

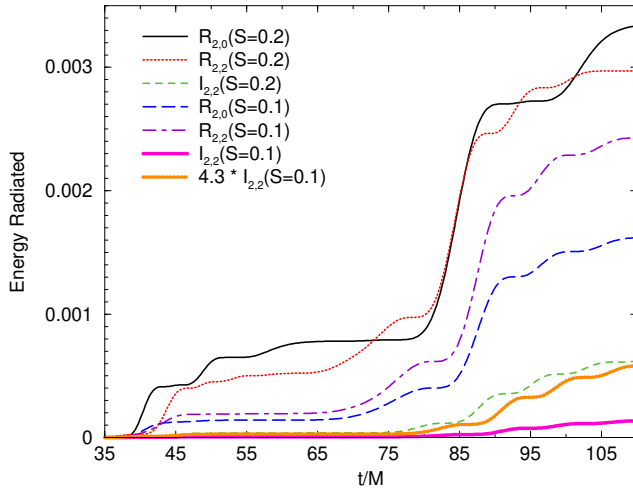


FIG. 7: The gravitational energy radiated up to time t as measured by an observer at $r = 35M$ for the $\ell = 2$ modes of the HS++ and MS++ configurations (for our configurations $R_{2,2} = R_{2-2}$, and $I_{2,2} = I_{2-2}$). The energy from the spurious initial burst leads to the first plateaus centered at $t = 60M$. These initial bursts of energy, while significant, are dominated by the total emitted radiation. We multiply $I_{2\pm 2}$ from the MS++ configuration ($S = 0.1M^2$) by 4.3 to demonstrate that quadratic (plus smaller higher-order terms) dependence of $I_{2\pm 2}$ on S .

and radiation properties of parallel and anti-parallel configurations. We plan to report the results of this spin up - spin down case leading to radiated *linear* momentum in a forthcoming paper.

These spinning-black-hole-binary scenarios were also studied in the complementary regime of the close limit approximation by Gleiser and Domínguez [40]. They examined the behavior of non-boosted, slowly rotating holes to second perturbative order. In that approximation the second-order terms proportional to the spin and the square of the proper distance, l , give rise to radiation of the angular momentum, J , proportional to the spin

$$J_{rad} \approx 0.0023(2S)(l/M)^4. \quad (18)$$

The analysis also predicts that the radiation of energy can be expanded as

$$\begin{aligned} \frac{E_{rad}}{M} \approx & 7.8 \times 10^{-4} (2S/M^2)^4 + 9.8 \times 10^{-5} (l/M)^4 \\ & - 2.8 \times 10^{-5} (2S/M^2)^2 (l/M)^2 \\ & + 1.3 \times 10^{-3} (2S/M^2)^2 (l/M)^4, \end{aligned} \quad (19)$$

The first term, being proportional only to S^4 , is generated by the radiation content of the BY initial data. The second term, proportional to l^4 , is the radiation for two non-spinning masses in a head-on collision. The third term is second-perturbative-order spin-orbit coupling term, and is the one that leads to the radiation of angular momentum.

V. DISCUSSION OF RESULTS

We have studied the spin-up of initially non-spinning and initially corotating black-hole binaries during the last stages of the inspiral orbital motion and found that it is much smaller than that needed to achieve tidal locking. This means that the time scale of tidal effects to spin up the black holes is much longer than the time scale for gravitational radiation to drive the merger (and hence increase the orbital frequency). This also implies that in an astrophysical scenario, black holes with low spin merge with essentially the same spin magnitude they had when the binary formed (note that Eq. (7) implies that $|\vec{S}| = 0$). We also note that it is this short timescale for gravitational radiation during the last few orbits that is responsible for the absence of an ISCO (innermost stable circular orbit) when the two holes have comparable masses. The concept of the ISCO arises naturally in the extreme mass ratio limit, where there is a cutoff between stable and unstable orbits. In this limit, the instability of orbits inside the ISCO is not driven by gravitational radiation, but by non-radiative terms in the particle's equation of motion. Thus the particle very slowly inspirals due to the emission of weak gravitational radiation, and then plunges when it reaches the ISCO. On the other hand, in the comparable mass regime, there is no such cutoff because gravitational radiation dominates the dynamics during the entire late-time inspiral and plunge phases.

In Fig. 8 we show the tracks of the horizon centroids in the S0 and SC configurations. Although coordinate dependent, the tracks help illustrate the lack of an ISCO in the comparable mass regime. Rather than showing an abrupt change near the last orbit, the tracks show a smooth increase in plunge velocity over the entire evolution. Note that the SC track is a tighter spiral than the S0 track, which is consistent with the results found previously by the authors [11]. Additional horizon tracks for multi-orbit non-spinning binaries can be found in Refs. [4, 5], while tracks for highly-spinning binaries can be found in Ref. [11].

After the merger, the final remnant black hole formed from the S0 configuration has a specific spin of $a/M_H = 0.688 \pm 0.001$ (where M_H is the remnant horizon mass) while remnant formed from the SC configuration has a specific spin of $a/M_H = 0.717 \pm 0.001$. Using these values in conjunction those found in Ref. [11] (see Table VI), we find (from a least-squares fit) that the specific spin of the final remnant horizon $(a/M_H)|_R$ varies with the initial specific spins of the two (equal-mass, equal-spin) black holes $(a/m)|_I$ according to:

$$\begin{aligned} (a/M_H)|_R = & 0.6879 + 0.2952 ((a/m)|_I) \\ & - 0.0374 ((a/m)|_I)^2, \end{aligned} \quad (20)$$

with an error of ± 0.001 in the range $(-0.757 < (a/m)|_I < 0.757)$. From this fit we extrapolate that the remnant horizon will have a specific spin no smaller

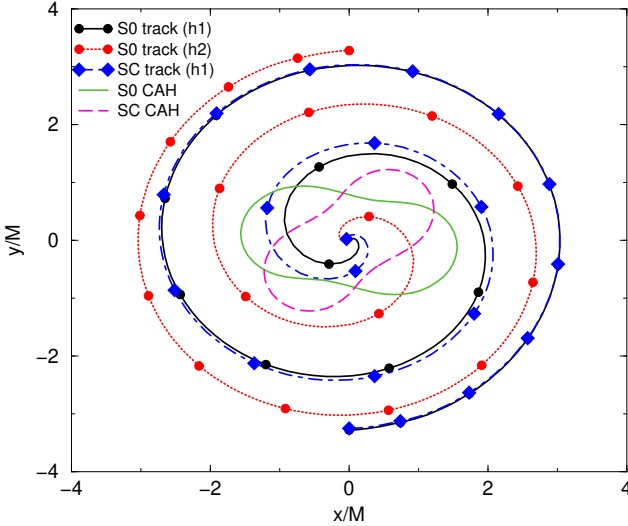


FIG. 8: The horizon tracks for the S0 and SC configurations with tick marks every $10M$ of evolution (we display only one of the SC tracks for clarity). Note that the S0 and SC tracks agree well for the first $100M$, and that after $100M$ the SC tracks show a tighter spiral and orbit longer before merging. The S0 configuration completes slightly less than 1.75 orbits, while the SC configuration completes slightly more.

than 0.355 (for the case of initially-maximal, anti-aligned spins) and no larger than $a/M_H = 0.946$ (for the case of initially-maximal, aligned spins), which supports our assertion in [11] that the cosmic censorship conjecture is not violated by the merger of two black holes. A least-squares fit of the energy radiated versus the initial individual spins yields

$$\frac{E_{rad}}{M} = 0.0348 + 0.0297((a/m)|_I) + 0.0170((a/m)|_I)^2, \quad (21)$$

with an error of ± 0.001 in the range $(-0.757 < (a/m)|_I < 0.757)$. Based on this fit we extrapolate that a quasi-circular binary will radiate no more than 8.1% of its mass during the final few orbits and merger.

We have also found that the tidal coupling in black-hole binaries responsible for the transfers of angular momentum from the individual spins to orbital is relatively small. Nevertheless, we have been able to compute this transfer with sufficient accuracy to model its dependence on the initial spin. We find that the radiated angular momentum, which is a measure of the angular momentum transferred from spin to orbit, has a linear-plus-cubic dependence on the initial spins; in qualitative agreement both with the post-Newtonian (see Eq. (16d)) and close-limit (see Eq. (18)) predictions. The radiated energy has a quadratic-plus-quartic dependence on the initial spin; again, in qualitative agreement with the post-Newtonian (see Eqs. (15)) and close-limit (see Eq. (19)) predictions.

Unfortunately the speculations of Price and Whe-

TABLE VI: The measured remnant horizon specific spin $(a/M_H)|_R$ and energy radiated E_{rad} , as well as the predicted remnant horizon specific spin $(a/M_H)|_{pred}$ and energy radiated $E_{rad}/M|_{pred}$ (based on a least-squares fit) for quasi-circular, equal-mass, equal-spin binaries with initial specific spins $(a/m)|_I$.

$(a/m) _I$	$(a/M_H) _R$	$(a/M_H) _{pred}$	E_{rad}/M	$E_{rad}/M _{pred}$
-0.757	0.443 ± 0.001	0.4430	$(2.2 \pm .01)\%$	2.20%
0.000	0.688 ± 0.001	0.6878	$(3.5 \pm 0.1)\%$	3.48%
0.1001	0.717 ± 0.001	0.7169	$(3.8 \pm 0.1)\%$	3.79%
0.757	0.890 ± 0.001	0.8900	$(6.7 \pm 0.2)\%$	6.70%
-1.0	***	0.355	***	2.2%
+1.0	***	0.946	***	8.1%

lan [41] suggesting this spin-up effect might be strong, and even dominant, are not confirmed by our computations. We see neither the possibility of a binary stalling by this effect nor the dominance of the $\ell = 3$ mode suggested in Ref. [41].

APPENDIX A: ISOLATED HORIZON SPIN AND HORIZON CIRCUMFERENCES

The most common technique for evaluating the spin of a numerically evolved black hole is to use the ratio of the polar to equatorial circumferences [42]. For a Kerr hole this ratio $C_r = C_p/C_{eq}$ is given by

$$C_r = \frac{1 + \sqrt{1 - (a/m)^2}}{\pi} E \left(-\frac{(a/m)^2}{(1 + \sqrt{1 - (a/m)^2})^2} \right), \quad (A1)$$

where a/m (m being the horizon mass) is the specific spin and $E(x)$ is the complete elliptic integral of the second kind. After a common horizon forms, C_r displays quasinormal ringing with a constant offset. To obtain the specific spin in finite time one uses a non-linear least-squares fit of C_r versus time to $C_r = C_0 + C_1 \exp[-C_2 t/M] \sin[C_3 t/M + C_4]$ to obtain C_0, \dots, C_4 (C_0 being the asymptotic value of C_r), and then a/m is obtained by inverting Eq. (A1). The authors have used this technique to obtain highly-accurate evaluations of the remnant spin in Refs. [2, 4, 11]. However, in the pre-merger case this technique is not accurate. There are two reasons for this. First, one cannot separate the large oscillations in C_r from the secular growth because the behavior of the oscillations is not known a-priori. Thus, there is a large error in the calculated spin. Second, the distortions on the horizon that lead to $C_r \neq 1$ are due to both the spin as well as tidal distortion of the horizon, and when the black holes are close, the tidal distortion dominate. Thus even if one can obtain an accurate measurement of the secular part of C_r , one would then need to disentangle the spin component of C_r from the tidal distortion component. Finally, the horizon circumference calculations are not coordinate invariant and lead

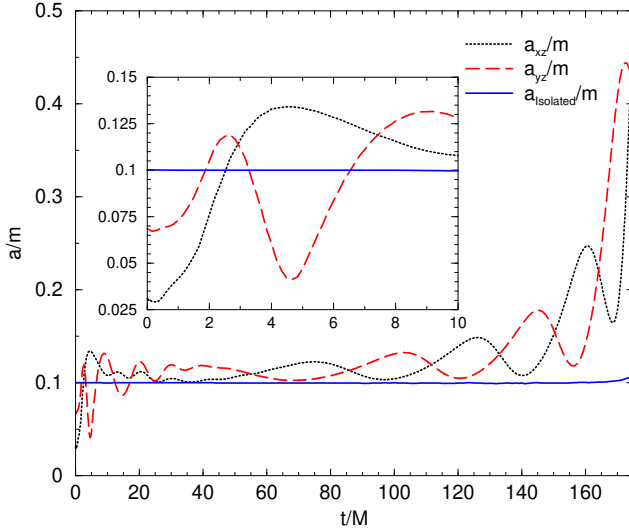


FIG. 9: The specific spin of the individual horizons for the SC orbiting binary configuration as calculated using the horizon circumferences and the isolated horizon technique. Here a_{xz} is obtained from C_{xz}/C_{eq} via Eq. (A1), a_{yz} from C_{yz}/C_{eq} . Note the large oscillations and secular growth in a_{xz} and a_{yz} compared to the much more accurate isolated horizon spin.

to errors when the coordinate are distorted (i.e. when the coordinate circles used in the calculations do not correspond to the correct coordinate circles in Boyer-Lindquist coordinates).

In Fig. 9 we show a/m for the SC orbiting-binary configuration calculated using the isolated horizon method and the circumference method. In the plot we show a/m

calculated using the ratios of the xz and yz polar circumferences to the equatorial (i.e. xy) circumference, as well a/m derived from the isolated horizon technique. Note that the initial values for the spin 0.03 and 0.07 for the two circumference-based calculations are significantly smaller than the expected 0.1, while the isolated horizon technique gives the correct value. The difference between the spin calculated from the two circumferences is a measure of the error. In this case that error is larger than the effect we want to measure. Note also that the spin derived from the circumferences shows a much stronger increase with time. This strong increase is driven by the increasing tidal distortion of the horizon (as can be inferred from the increase in amplitude of the oscillations).

ACKNOWLEDGMENTS

We thank Bernard Kelly for careful reading of this text. We thank Erik Schnetter for providing the Cactus thorns to implement Pi-symmetry boundary conditions, Marcus Ansorg for providing the TwoPUNCTURES thorn, and Badri Krishnan for suggesting the comparison between the isolated horizon technique and the horizon circumference technique. We gratefully acknowledge the support of the NASA Center for Gravitational Wave Astronomy at University of Texas at Brownsville (NAG5-13396) and the NSF for financial support from grants PHY-0140326 and PHY-0354867. Simulations were performed on the 70-node ‘Funes’ cluster at UTB, on the ‘Lonestar2’ supercomputer at TACC, and on the ‘Tungsten’ supercomputer at NCSA.

[1] F. Pretorius, Phys. Rev. Lett. **95**, 121101 (2005), gr-qc/0507014.
[2] M. Campanelli, C. O. Lousto, P. Marronetti, and Y. Zlochower, Phys. Rev. Lett. **96**, 111101 (2006), gr-qc/0511048.
[3] J. G. Baker, J. Centrella, D.-I. Choi, M. Koppitz, and J. van Meter, Phys. Rev. Lett. **96**, 111102 (2006), gr-qc/0511103.
[4] M. Campanelli, C. O. Lousto, and Y. Zlochower, Phys. Rev. D **73**, 061501(R) (2006).
[5] J. G. Baker, J. Centrella, D.-I. Choi, M. Koppitz, and J. van Meter, Phys. Rev. D **73**, 104002 (2006), gr-qc/0602026.
[6] F. Pretorius (2006), gr-qc/0602115.
[7] M. A. Scheel et al. (2006), gr-qc/0607056.
[8] M. Campanelli, Class. Quant. Grav. **22**, S387 (2005), astro-ph/0411744.
[9] F. Herrmann, D. Shoemaker, and P. Laguna (2006), gr-qc/0601026.
[10] J. G. Baker et al. (2006), astro-ph/0603204.
[11] M. Campanelli, C. O. Lousto, and Y. Zlochower, Phys. Rev. D **74**, 041501(R) (2006), gr-qc/0604012.
[12] M. Caudill, G. B. Cook, J. D. Grigsby, and H. P. Pfeiffer, Phys. Rev. D **74**, 064011 (2006), gr-qc/0605053.
[13] L. Blanchet, Phys. Rev. D **65**, 124009 (2002), gr-qc/0112056.
[14] P. Grandclément, E. Gourgoulhon, and S. Bonazzola, Phys. Rev. D **65**, 044021 (2002), gr-qc/0106016.
[15] L. Bildsten and C. Cutler, Astrophys. J. **400**, 175 (1992).
[16] C. S. Kochanek, Astrophys. J. **398**, 234 (1992).
[17] P. Marronetti and S. L. Shapiro, Phys. Rev. D **68**, 104024 (2003), gr-qc/0306075.
[18] S. Brandt and B. Brügmann, Phys. Rev. Lett. **78**, 3606 (1997), gr-qc/9703066.
[19] M. Ansorg, B. Brügmann, and W. Tichy, Phys. Rev. D **70**, 064011 (2004), gr-qc/0404056.
[20] cactus_web, cactus Computational Toolkit home page: <http://www.cactuscode.org>.
[21] Y. Zlochower, J. G. Baker, M. Campanelli, and C. O. Lousto, Phys. Rev. D **72**, 024021 (2005), gr-qc/0505055.
[22] T. Nakamura, K. Oohara, and Y. Kojima, Prog. Theor. Phys. Suppl. **90**, 1 (1987).
[23] M. Shibata and T. Nakamura, Phys. Rev. D **52**, 5428 (1995).

- [24] T. W. Baumgarte and S. L. Shapiro, Phys. Rev. D **59**, 024007 (1999), gr-qc/9810065.
- [25] U. Sperhake (2006), gr-qc/0606079.
- [26] M. Hannam, S. Husa, D. Pollney, B. Brügmann, and N. O'Murchadha (2006), gr-qc/0606099.
- [27] M. Alcubierre, B. Brügmann, P. Diener, M. Koppitz, D. Pollney, E. Seidel, and R. Takahashi, Phys. Rev. D **67**, 084023 (2003), gr-qc/0206072.
- [28] C. Gundlach and J. M. Martin-Garcia, Phys. Rev. D**74**, 024016 (2006), gr-qc/0604035.
- [29] J. Thornburg, Class. Quantum Grav. **21**, 743 (2004), gr-qc/0306056.
- [30] O. Dreyer, B. Krishnan, D. Shoemaker, and E. Schnetter, Phys. Rev. D **67**, 024018 (2003), gr-qc/0206008.
- [31] A. Ashtekar and B. Krishnan, Phys. Rev. D **68**, 104030 (2003), gr-qc/0308033.
- [32] M. Koppitz, Ph.D. thesis, Universität Potsdam (2004).
- [33] P. Diener et al., Phys. Rev. Lett. **96**, 121101 (2006), gr-qc/0512108.
- [34] J. Baker, M. Campanelli, C. O. Lousto, and R. Takahashi, Phys. Rev. D **65**, 124012 (2002), astro-ph/0202469.
- [35] L. E. Kidder, Phys. Rev. D **52**, 821 (1995), gr-qc/9506022.
- [36] C. M. Will, Phys. Rev. D**71**, 084027 (2005), gr-qc/0502039.
- [37] M. Campanelli, B. Kelly, and C. O. Lousto, Phys. Rev. D **73**, 064005 (2006), gr-qc/0510122.
- [38] S. Dain, Phys. Rev. Lett. **87**, 121102 (2001), gr-qc/0012023.
- [39] S. Dain, Phys. Rev. D**64**, 124002 (2001), gr-qc/0103030.
- [40] R. J. Gleiser and A. E. Dominguez, Phys. Rev. D**65**, 064018 (2002), gr-qc/0109018.
- [41] R. H. Price and J. T. Whelan, Phys. Rev. Lett **87**, 231101 (2001), gr-qc/0107029.
- [42] M. Alcubierre et al., Phys. Rev. D **72**, 044004 (2005), gr-qc/0411149.
- [43] Very rarely our isolated horizon routine fails to find the correct approximate Killing vector and gives a very inaccurate value for the spin. When this happens (we observes this no more than once per run for these orbital runs and never for the head-on runs below) we drop the data point.